RSC Advances

PAPER

Cite this: *RSC Adv.*, 2024, **14**, 6883

Enhancement in the dielectric and magnetic properties of Ni^{2+}–Cu^{2+} co-doped $BaFe_{11}Cu_{1-x}Ni_xO_{19}$ hexaferrites ($0.0 \leq x \leq 1.0$)

M. Atif, *[a] H. Ul Husnain,[a] Atta Ur Rehman, [ab] U. Younas,[a] T. Rafique,[a] W. Khalid,[a] Z. Ali [a] and M. Nadeem[c]

Herein, Ni^{2+}–Cu^{2+} co-doped barium hexaferrites ($BaFe_{11}Cu_{1-x}Ni_xO_{19}$, $0.0 \leq x \leq 1.0$ with an interval of 0.25) were successfully synthesized using a co-precipitation method. The formation of a magnetoplumbite structure with the $P6_3/mmc$ space group was confirmed by Rietveld refinement of the obtained X-ray diffraction patterns. Microstructural investigations revealed grains in the shape of hexagonal plates, while co-doping resulted in a variation in the grain sizes of the prepared samples. X-ray photoelectron spectroscopy was performed to determine the valence state of iron in the prepared hexaferrites. Impedance spectroscopy analysis revealed that dielectric permittivity initially decreased with an increase in the co-dopant content up to $x = 0.5$ and then increased by two orders of magnitude for $x = 1.0$. Alternatively, resistive properties showed microstructural resistance values in the range 10^5–10^8 Ω, with the highest value obtained for the sample with $x = 0.5$. Furthermore, magnetic measurements indicated that all the prepared samples exhibited ferrimagnetic behaviour. Saturation magnetization and magnetic anisotropy values were found to be the highest for the sample with $x = 1.0$, which also had the lowest coercivity among the prepared samples. Herein, the observed variations in the obtained results can be explained by the variations in grain sizes and the Fe^{2+}/Fe^{3+} ratio associated with the preferential occupation of co-dopants at octahedral sites. Based on our findings, the $BaFe_{11}Ni_1O_{19}$ ($x = 1.0$) composition appears to be the most promising choice as a microwave absorption material among the prepared samples owing to the coexistence of high dielectric permittivity (>10^3 at 10^7 Hz) and saturation magnetization (73 emu g^{-1}).

Received 1st October 2023
Accepted 13th February 2024

DOI: 10.1039/d3ra06684c

rsc.li/rsc-advances

1. Introduction

Presently, hexaferrites are one of the most extensively investigated materials because of their wide range of practical application in fields such as magnetic shielding, mobile communication, electronic devices, magnetic biosensors, magnetic recording devices, and stealth technologies.[1,2] Generally, hexaferrites have a more complicated structure compared to spinel ferrites and orthoferrites and are a very important class of permanent magnets. Based on the chemical composition and crystalline structure of hexaferrites, they can be divided into six different types.[3] Among them, M-type hexaferrites ($MeO \cdot 6Fe_2O_3$, where Me is Ba, Sr, or Pb) are the most significant type of hexaferrites owing to their remarkable properties, which include high coercivity, high permittivity, high permeability, and high values of isotropic constants as well as its chemical stability and high corrosion resistance.[4] The crystal structure of an M-type hexaferrite is composed of a combination of $R = Me^{2+}Fe_6^{3+}O_{11}^{2-}$, $S = Fe_6^{3+}O_8^{2-}$, R*, and S* blocks, where R* and S* are 180° inversion of the R and S block, respectively, along the hexagonal *c*-axis.[3] One unit cell of M-type hexaferrites is made up of two molecules, and each molecule contains five layers of oxygen atoms. There is a total of 64 ions in each unit cell, including two heavy metal divalent cations, 38 oxygen ions, and 24 ferric ions. The presence of ferric (Fe^{3+}) ions imparts magnetism to this type of hexaferrite. In each sublattice of M-type hexaferrites, there are a total of 12 ferric ions occupying five distinct interstitial sites, namely 12k, $4f_2$, $4f_1$, 2a, and 2b. Six of these 12 ferric ions occupy a 12k (octahedral) site with a positive spin. On $4f_2$ (octahedral) and $4f_1$ (tetrahedral) sites, there are two ferric ions with spin-down. On 2a (octahedral) and 2b (trigonal bipyramidal) sites with spin-up, there is one ferric ion.[3] In total, eight of the twelve ferric ions have spin-up, while four have spin-down. This indicates that after balancing with four spin-down ferric ions, there are still four spin-up ferric ions.[5] These four spin-up ferric ions contribute to the total magnetic moment of M-type hexaferrite. Iron (Fe) is a d-block element with five unpaired electrons in its outermost

[a]*Functional Materials Lab, Department of Physics, Air University, PAF Complex E-9, Islamabad, Pakistan. E-mail: matif@mail.au.edu.pk*

[b]*Department of Physics, The University of Hong Kong, Pokfulam, Hong Kong*

[c]*Polymer Composite Group, Physics Division, Directorate of Science, PINSTECH, P.O. Nilore, Islamabad, Pakistan*

orbit, resulting in a magnetic moment of 5 μ_B for each ferric ion. Due to the presence of four spin-up ferric ions in each unit cell of hexaferrite, the net magnetic moment of each cell is 20 μ_B.[6]

Among the M-type hexaferrite materials, barium hexaferrite ($BaFe_{12}O_{19}$) has attracted considerable interest from researchers due to its outstanding dielectric and magnetic properties, which make it useful as an electromagnetic wave absorber.[7,8] When electromagnetic waves interact with microwave absorbers, the energy of the incident wave is absorbed by the absorbers. At the ferromagnetic resonance frequency, this energy absorption is at its maximum. The ideal choice for a microwave absorber is a material that can both absorb high-energy waves and respond quickly to incident radiation. Typically, the absorption of an incident waves by a material depends on its dielectric permittivity (ε'), saturation magnetization (M_s), and the magnitude of its response to an incident wave, which is defined by its coercivity (H_c). Thus, if a material has a high ε' and M_s with a low H_c, it may act as a microwave absorber. Given that $BaFe_{12}O_{19}$ has a high values of ε' and M_s but an equally strong H_c, it is inappropriate for use in microwave absorber applications. This problem can be solved by substituting transition metal cations for Ba^{2+} or Fe^{3+} ions in $BaFe_{12}O_{19}$, which reduces the H_c value of the material and improves its magnetic and microwave-absorbing properties.[9] Manglam *et al.* explored the magnetic properties of Zn^{2+}-doped $BaFe_{12-x}Zn_xO_{19}$ hexaferrites.[10] They found that the maximum M_s and minimum H_c values were obtained for $x = 0.2$, which were described in terms of the lattice strain and super-exchange interaction, respectively. Behera *et al.* investigated the impact of Ni^{2+} doping on the magnetic and dielectric characteristics of $BaFe_{12-x}Ni_xO_{19}$.[11] According to them, the dielectric constant was found to increase with an increase in the Ni^{2+} doping content, while the values of M_s and H_c decreased with Ni^{2+} doping. Wang *et al.* reported the coexistence of remarkable improvements in the dielectric and magnetic characteristics of Ni^{2+}-doped $BaFe_{12-x}Ni_xO_{19}$ hexaferrites due to the presence of more Fe^{2+}/Fe^{3+} pair dipoles and the preferential occupancy of Ni^{2+} ions at the $4f_2$ sites.[12] Kumar *et al.* explored the effect on Cu^{2+} doping on the properties of $BaFe_{12-x}Cu_xO_{19}$ hexaferrites.[13] According to them, a correlation was established between the structural parameters and magnetic/dielectric properties, and they found the maximum M_s, minimum H_c, and high dielectric constant for the $x = 1.0$ sample. To further improve the magnetic and microwave-absorbing properties of barium hexaferrites, co-doping of Ni^{2+} with a combination of some other divalent metal ions has been reported in the literature. Widyastuti *et al.* reported that the magnetic properties of barium hexaferrite can be significantly improved by doping Ni^{2+} and Zn^{2+} ions in place of Fe^{3+}.[14] They found that the highest M_s (95 emu g^{-1}) and the lowest H_c (0.12 T) were obtained for $x = 0.6$ among the $BaFe_{12-2x}Ni_xZn_xO_{19}$ hexaferrites prepared at pH = 11 and sintered at 1050 °C. Moreover, Susilawati *et al.* found that the values of M_s and ε' increased, while the H_c value decreased with an increase in the co-dopant contents in $BaFe_{12-2x}Ni_xCo_xO_{19}$ hexaferrites.[15] However, the maximum reflection loss of −14.47 dB together with an absorption coefficient of 96.43% was achieved for the $x = 1.0$ sample. Hence, based on the above-mentioned literature, we found that the coexistence of high dielectric and magnetic characteristics in co-doped barium hexaferrites makes these materials potential candidates as high-performance microwave absorbers.

In this work, divalent transition metals such as Ni^{2+} and Cu^{2+} were utilized as a replacement for Fe^{3+} in M-type barium hexaferrites to alter their magnetic and dielectric characteristics because of their close ionic radii and electronic configuration. Moreover, the replacement of Fe^{3+} by the lower valence of Ni^{2+}–Cu^{2+} ion pair may generate extra charge carriers for conduction, leading to high dielectric permittivity in barium hexaferrites. Further, it is anticipated that the magnetic nature of this ion pair will maintain the magnetic interactions, which may enhance the magnetization and reduce the coercivity depending on their preferential occupation of the octahedral sites in M-type hexaferrites.[13,16] Therefore, different compositions of $BaFe_{11}Cu_{1-x}Ni_xO_{19}$ hexaferrites with $x = 0.0$, 0.25, 0.50, 0.75, and 1.0 were prepared using the co-precipitation method, and then investigated for their microstructural, magnetic, and dielectric characteristics. Based on the obtained results, we found the coexistence of considerable high saturation magnetization (50–73 emu g^{-1}) and dielectric permittivity ($\sim 10^3$–10^5@10 Hz) in the prepared samples.

2. Experimental details

The co-precipitation method was used to synthesize Ni^{2+}-doped $BaFe_{11}Cu_{1-x}Ni_xO_{19}$ with $x = 0.0$, 0.25, 0.50, 0.75, and 1.0. The precursors used for the synthesis of the above-mentioned samples were barium nitrate [$Ba(NO_3)_2$, Sigma-Aldrich, 99%], ferric nitrate [$Fe(NO_3)_3 \cdot 9H_2O$, Alfa-Aesar, 99%], copper nitrate [$Cu(NO_3)_2 \cdot 2.5H_2O$, Sigma-Aldrich, ≥98%], nickel nitrate [$Ni(NO_3)_2 \cdot 6H_2O$, Sigma-Aldrich, ≥98%], potassium hydroxide [KOH, Sigma-Aldrich, 90%], and deionized water. Initially, stoichiometric quantities of nitrates were mixed in 100 mL deionized water and stirred for 15 min on a hot plate under magnetic stirring. The mixed solution of nitrates was incorporated dropwise into 100 mL solution of KOH. Subsequently, the mixture was stirred for 2 h at 80 °C on the hotplate, and then precipitates were formed. After multiple washings with deionized water, the samples were dried in an oven for 8 h at 100 °C. These dried samples were manually crushed into a fine powder using a mortar and pestle, and then annealed for 12 h at 1000 °C. The annealed powders were compressed under a compaction pressure of 5 tons per cm^2 using a hydraulic press to produce pellets. Finally, the pelletized samples were sintered for 6 h at 1200 °C in a furnace.

X-ray diffraction (ARL EQUINOX 3000) was performed to determine the structural phase of the prepared samples using Cu-Kα radiation with a wavelength of $\lambda = 1.5418$ Å. The machine was operated at a voltage of 40 kV/30 mA to observe the peaks in the 2θ range of 10° to 70°. Scanning electron microscopy (Hitachi S4800, FE-SEM) was used to study the surface morphology of the prepared samples. Energy dispersive X-ray spectroscopy (Oxford Instruments X-Max 80) was utilized to study the elemental compositional analysis of the prepared samples. To characterize the valence state of iron in the prepared hexaferrites, X-ray photoelectron spectroscopy was

performed using a SPECS PHOIBOS 100 instrument working at 1486.6 eV (Al K_α). An Alpha-N Analyzer (Novocontrol, Germany) was used to investigate the dielectric properties at room temperature. The magnetic properties were measured at room temperature using a magnetic measurement system (MPMS XL-7, Quantum Design Corporation, USA).

3. Results and discussion

The X-ray diffraction patterns of the Ni^{2+}-doped $BaFe_{11}Cu_{1-x}Ni_xO_{19}$ hexaferrites with $x = 0.0$, 0.25, 0.50, 0.75, and 1.0 are displayed in Fig. 1(a–e), respectively. As can be seen, all the produced samples exhibit XRD patterns corresponding with the

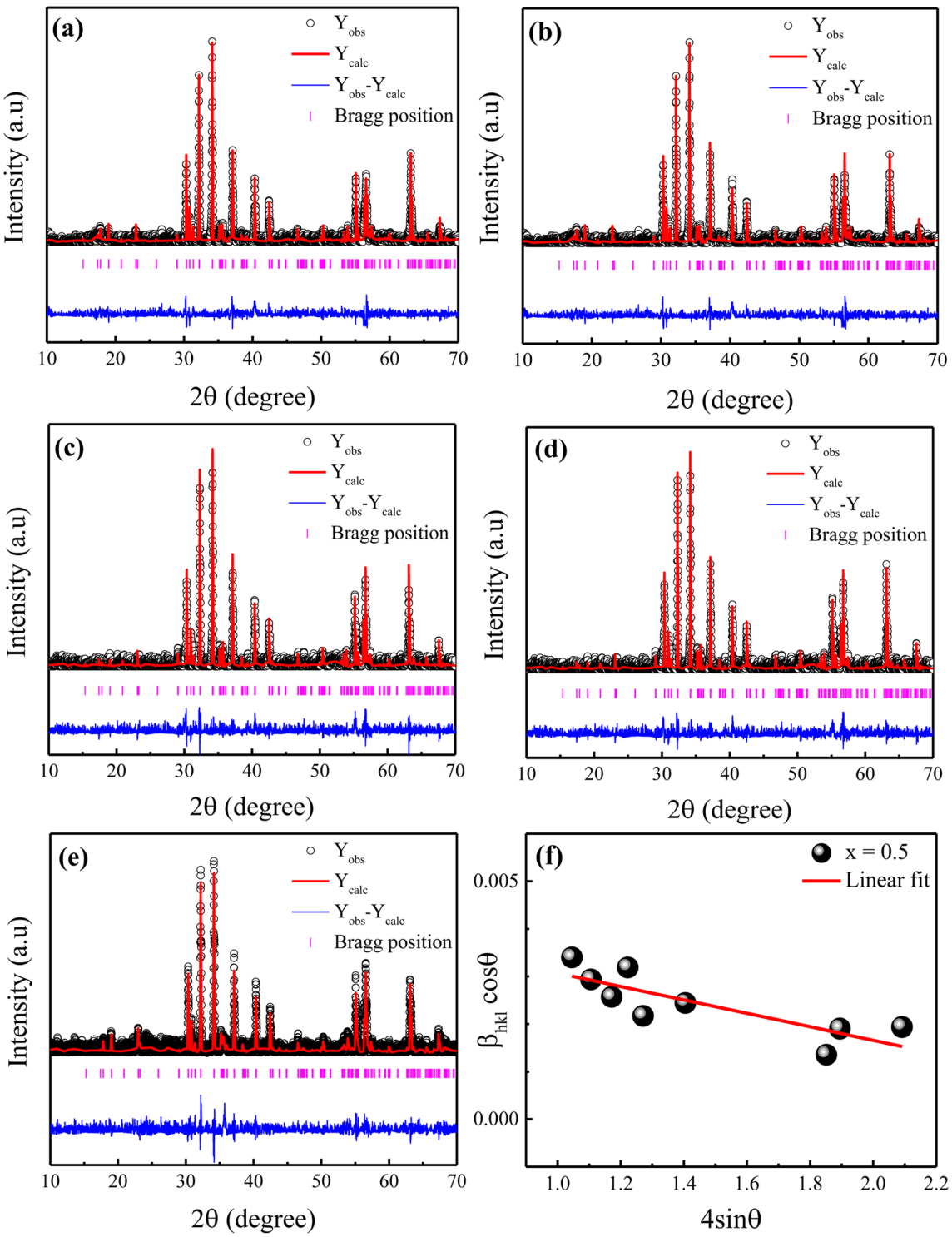

Fig. 1 (a–e) Rietveld refinement of the XRD data for Ni^{2+}-substituted $BaFe_{11}Cu_{1-x}Ni_xO_{19}$ hexaferrites with $x = 0.0$, 0.25, 0.5, 0.75, and 1.0, and (f) representative Williamson–Hall plot between $\beta_{hkl}\cos\theta$ *versus* $4\sin\theta$ for the $x = 0.5$ sample.

Table 1 Variation in lattice parameters (*a*,*c*, and *c*/*a*), unit-cell volume (V), goodness of fit (χ^2), crystallite size (d), lattice strain (ε), and grain size (G) with x in $BaFe_{11}Cu_{1-x}Ni_xO_{19}$ hexaferrites

Sample (x)	a (Å)	c (Å)	c/a	V (Å)^3	χ^2	d (nm)	ε ($\times10^{-3}$)	G (μm)
0.0	5.907	23.250	3.936	702.54	1.35	61	0.76	2.14
0.25	5.902	23.240	3.937	701.05	1.34	55	1.11	1.53
0.5	5.891	23.207	3.939	697.45	1.63	40	1.69	1.09
0.75	5.895	23.241	3.942	699.42	1.55	48	0.99	1.81
1.0	5.899	23.270	3.944	701.24	1.35	56	0.93	2.03

standard JCPDS File No. 00-039-1433 for the M-type hexagonal structure with the $P6_3/mmc$ space group.[17] Moreover, the XRD patterns demonstrate the absence of typical impurity peaks for all the samples, confirming the phase purity of the produced samples. The FullProf software was used to perform Rietveld structural refinements on the XRD patterns of the produced samples. The peak profiles were refined using the pseudo-Voigt function and the background was fitted using a polynomial with six coefficients. The structural parameters were refined until they approached a goodness of fit (χ^2) value of close to 1.0. Here, the small goodness of fit values (χ^2 = 1.30–1.63) confirm that the structural parameters are accurate. The estimated refined values of the lattice constants (*a*,*c*), unit-cell volume (V), and goodness of fit (χ^2) are listed in Table 1. It can be seen that the estimated values of lattice parameters for the $BaFe_{11}Cu_1O_{19}$ hexaferrites ($x = 0.0$) are $a = 5.9058$ Å and $c = 23.270$ Å, which are consistent with the reported work.[13] However, these values are found to be higher than the respective values of $a = 5.887$ Å and $c = 23.203$ Å for the pure $BaFe_{12}O_{19}$ sample prepared under similar conditions (not shown here).[18] The possible reason for the observed increase in the lattice parameters of $x = 0.0$ is due to the replacement of Fe^{3+} with a smaller ionic radius (0.645 Å) by Cu^{2+} ions with a larger ionic radius (0.73 Å).[19] Moreover, with an increase in the Ni^{2+} doping content (x) in the $BaFe_{11}Cu_{1-x}Ni_xO_{19}$ hexaferrites, the values of the lattice parameters (*a*,*c*) were found to decrease up to $x = 0.5$, and then increase with a further increase in the content of Ni^{2+} ions (*i.e.*, $x > 0.5$). This variation in the lattice constants can be ascribed to the difference in the ionic radii of the dopant Ni^{2+} (0.69 Å) ions compared to Fe^{3+} (0.645 Å) and Cu^{2+} (0.73 Å), valence change of Fe^{3+} to Fe^{2+}, and the site occupancy of Cu^{2+}/Ni^{2+} ions in the hexagonal unit-cell. Here, the initial decrease in the lattice parameters of the $BaFe_{11}Cu_{1-x}Ni_xO_{19}$ samples up to $x = 0.5$ can be attributed to the replacement of the Cu^{2+} ions from their preferable $4f_2$ site[20] by the Ni^{2+} ions at the 12k and $4f_2$ sites.[12] This is because in an octahedral field, the ionic radius of Ni^{2+} (0.69 Å) is smaller than that of Cu^{2+} (0.73 Å), resulting in a decrease in the lattice parameters. However, for $x > 0.5$, the effect of forming oxygen vacancies to balance the charge neutrality has a greater effect on the lattice parameters than the effect of replacing Fe^{3+} ions in the lattice with Cu^{2+} and Ni^{2+}, resulting in an increase in the Fe^{2+} ions (will be discussed later in detail). The ionic radius of Fe^{2+} at the octahedral site is 0.78 Å, which is found to be larger than that of the $Cu^{2+}/Ni^{2+}/Fe^{3+}$ ions, resulting in an increase in the lattice constant values. Further, the observed variation in the unit-cell volume (V) is consistent with the changes in the lattice parameters of the produced samples, as can be seen in Table 1. Alternatively, the *c*/*a* ratio of the prepared hexaferrite samples was found to be less than 3.98, indicating the presence of an M-type hexagonal structure.[21] Further, the Williamson–Hall method was employed to estimate the average crystallite size (d) and lattice strain (ε) of the Ni^{2+}-doped $BaFe_{11}Cu_{1-x}Ni_xO_{19}$ hexaferrites with $x = 0.0$, 0.25, 0.50, 0.75, and 1.0, which is defined as follows:[22]

$$\beta_{hkl}\cos\theta = \frac{k\lambda}{d} + 4\varepsilon\sin\theta \quad (1)$$

where β_{hkl} is the FWHM of the diffraction peak, θ is the Bragg angle, k is a constant, λ is the wavelength of the X-ray, and d is the average crystallite size. Fig. 1(f) displays the plot of $\beta_{hkl}\cos\theta$ *vs.* $4\sin\theta$ for the prepared sample with $x = 0.5$. According to this representative plot, the slope of the straight line provides the lattice strain (ε) in the prepared hexaferrites, while the *y*-intercept provides the average crystallite size (d). A similar procedure was also followed for the other samples (not shown here). The calculated values of ε and d for the produced samples are presented in Table 1. It was found that with an increase in the Ni^{2+} doping content, the value of d decreased from 61 nm ($x = 0.0$) to 40 nm ($x = 0.5$), and then increased to 56 nm ($x = 1.0$). In contrast, the value of ε initially increased with an increase in the Ni^{2+} doping content up to $x = 0.5$, which can be attributed to the replacement of Cu^{2+} by Ni^{2+} ions with a smaller ionic radius. However, for a higher Ni^{2+} content ($x > 0.5$), the observed decrease in the value of ε can be attributed to the creation of defects (oxygen vacancies) at the octahedral sites, which caused the unit-cell volume to expand slightly, and then reduced the distortion in the hexaferrite structure.

The surface morphological analysis of the Ni^{2+}-doped $BaFe_{11}Cu_{1-x}Ni_xO_{19}$ hexaferrites with $x = 0.0$, 0.25, 0.50, 0.75, and 1.0 was studied using scanning electron microscopy (FE-SEM). Fig. 2(a–e) demonstrate the SEM micrographs of the prepared hexaferrites, respectively, which were taken from the fractured surfaces of the pelletized samples sintered for 6 h at 1200 °C. The FE-SEM images show that all samples exhibit a heterogeneous distribution of grain sizes, with the majority of grains possessing a hexagonal shape and different sizes. The ImageJ software was used to determine the average grain size (G) and the results are listed in Table 1. The grain size was found to decrease with an increase in Ni^{2+} doping concentration up to $x = 0.5$, and then it increased. Here, the variation in grain size with Ni^{2+} doping in the $BaFe_{11}Cu_{1-x}Ni_xO_{19}$ hexaferrites can be attributed to several factors, such as the difference in the ionic radius, strain, porosity, and microstructural features, which can interact and influence each other. The initial decrease in grain size with an increase in the Ni^{2+} concentration can be due to the increase in the lattice strain caused by the mismatch in ionic radius, which hinders the grain growth.[10] However, at higher doping concentrations ($x > 0.5$), the grain size may increase due to the agglomeration of grains, relaxation of strain, and lattice expansion. Fig. 2(f) displays the result of energy dispersive X-ray spectroscopy (EDX) performed on a representative

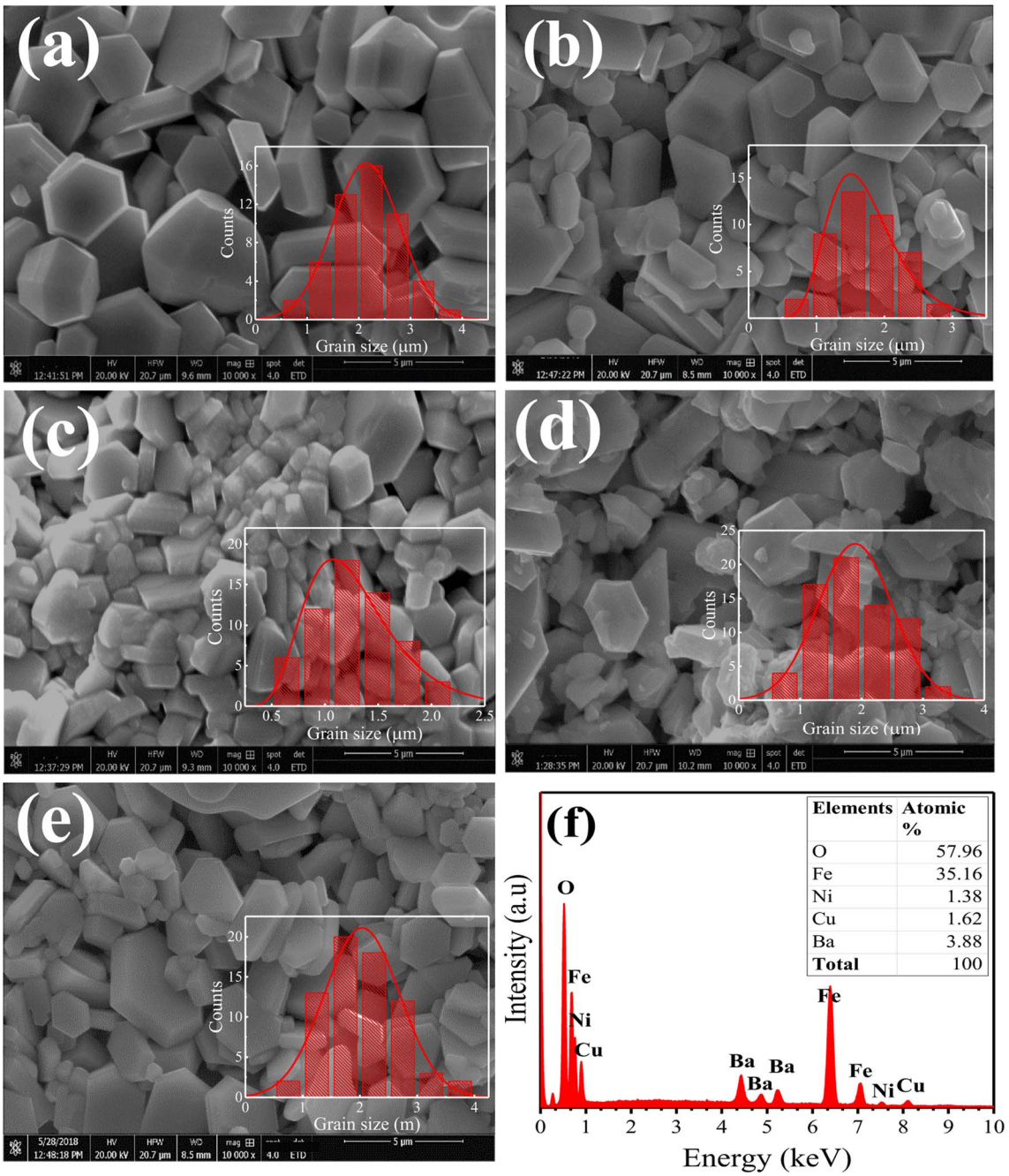

Fig. 2 (a–e) FESEM images of $BaFe_{11}Cu_{1-x}Ni_xO_{19}$ hexaferrites with $x = 0.0$, 0.25, 0.5, 0.75, and 1.0, and (f) EDX spectrum of a representative sample with $x = 0.5$. Insets in (a–e) show the grain size distribution in the prepared samples, while the inset in (f) presents the elemental ratios of $x = 0.5$ composition in atomic%.

$BaFe_{11}Cu_{0.5}Ni_{0.5}O_{19}$ ($x = 0.5$) sample. The EDX spectrum only shows the spectral lines of Ba, Fe, Cu, Ni and O, indicating the phase purity of the material. The inset of the figure shows the atomic proportions of each element, indicating that the prepared sample has a stoichiometric ratio for each ion, which is identical to the $BaFe_{11}Cu_{0.5}Ni_{0.5}O_{19}$ sample.

Fig. 3(a) displays a representative X-ray photoelectron spectroscopy (XPS) survey spectrum for the prepared $BaFe_{11}Cu_{1-x}Ni_xO_{19}$ hexaferrites with $x = 0.75$. The spectrum exclusively reveals peaks associated with the C, Ba, Fe, Cu, Ni, and O elements.[23] The C 1s peak at 284.8 eV can be attributed to contaminating carbon. The location of this peak was utilized to calibrate the binding energies of all of the other elements. All other samples exhibited comparable survey spectra (not shown here). The binding energy of each element proves that the prepared hexaferrites have a single-phase, without any additional impurity phases. Fig. 3(b) shows the high-resolution XPS spectrum of Fe 2p for the sample with $x = 0.75$, which was

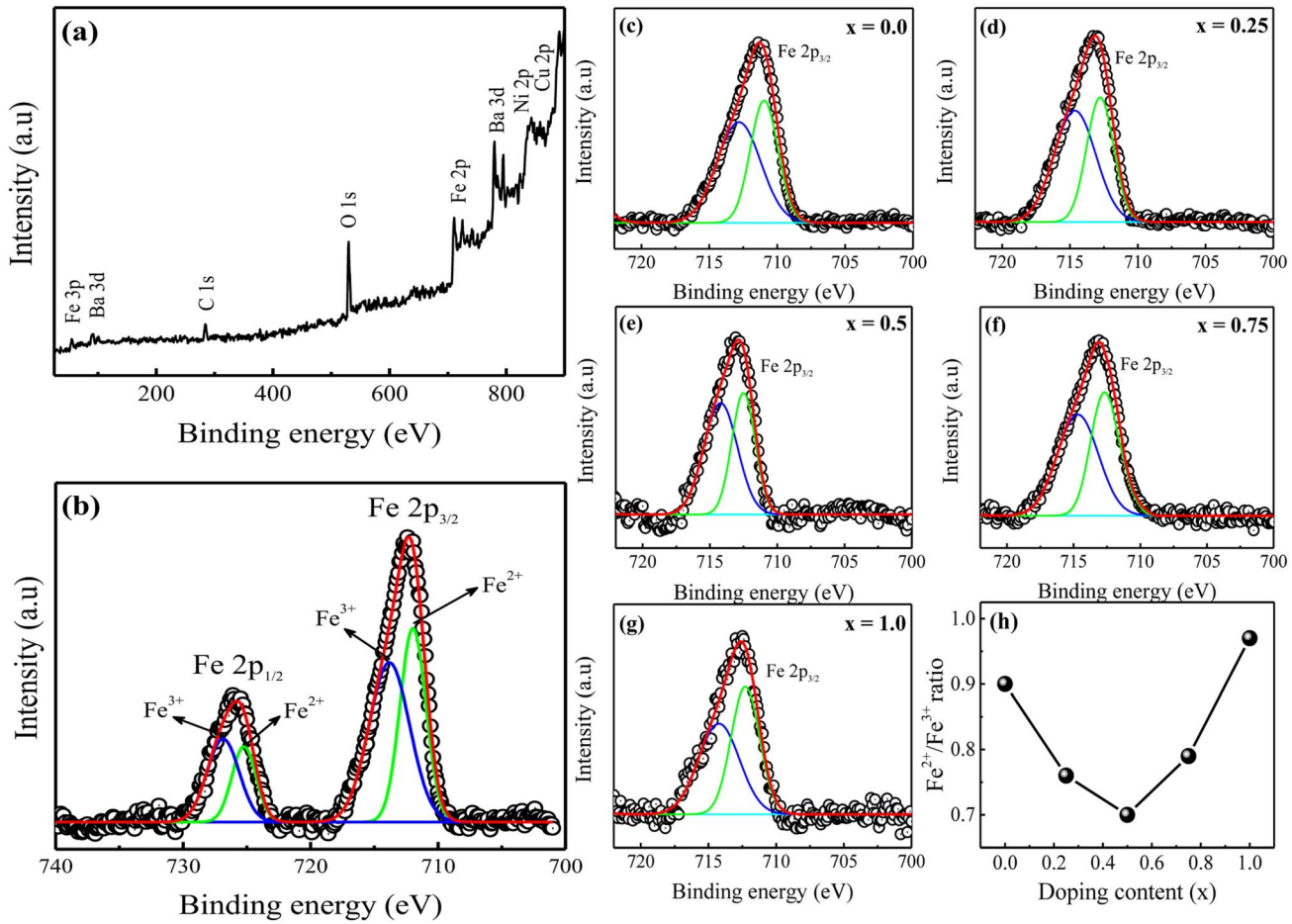

Fig. 3 (a) XPS survey spectrum and (b) high-resolution XPS spectrum of Fe 2p for the $x = 0.75$ sample. (c–g) Fe $2p_{3/2}$ XPS spectra of the prepared $BaFe_{11}Cu_{1-x}Ni_xO_{19}$ hexaferrites with $x = 0.0$–1.0. (h) Variation in Fe^{2+}/Fe^{3+} ratio with doping content.

obtained with a small energy step size. Here, the two peaks with binding energies of 712.2 eV and 725.6 eV correspond to Fe $2p_{3/2}$ and Fe $2p_{1/2}$ of the Fe species, respectively.[16] These peaks were deconvoluted into two peaks, with the first peak representing the valence state of Fe^{2+} and the subsequent peak representing the Fe^{3+} state. Each fitting peak in the spectrum of Fe 2p was considered to have the form of a Lorentzian–Gaussian distribution. Moreover, the relative area of the corresponding peaks can be used to determine the ratio of Fe ions with the Fe^{2+} valence state to that with Fe^{3+}. Fig. 3(c–g) illustrate the comparative Fe $2p_{3/2}$ XPS spectra of the prepared $BaFe_{11}Cu_{1-x}Ni_xO_{19}$ hexaferrites with $x = 0.0$–1.0. Based on the analysis, it was observed that the Fe^{2+}/Fe^{3+} ratio decreased as the concentration of Ni^{2+} doping increased until $x = 0.5$, after which it increased significantly (see Fig. 3(h)). This behavior can be attributed to the fact that hexaferrites sintered in air often possess intrinsic oxygen vacancies and Fe^{2+} ions,[12] which can be altered upon Ni^{2+} doping. The subsequent section will provide a comprehensive analysis of the impact of Ni^{2+} doping on the predicted Fe^{2+}/Fe^{3+} ratio, which is a crucial factor in determining the conduction mechanism of hexaferrites, and may consequently alter the electrical properties of the prepared samples.

Fig. 4(a) shows the behaviour of the real part of dielectric permittivity (ε') *versus* applied frequency for the produced Ni^{2+}-doped $BaFe_{11}Cu_{1-x}Ni_xO_{19}$ hexaferrites with $x = 0.0$, 0.25, 0.50, 0.75, and 1.0 measured at room temperature. Typically, the dielectric polarization in pure $BaFe_{12}O_{19}$ is determined by the exchange of charges between the $Fe^{2+} \leftrightarrow Fe^{3+}$ ions at the octahedral site, while the Fe^{2+}/Fe^{3+} ratio is determined by the conversion of dominant Fe^{3+} to Fe^{2+} *via* doping, sintering, and environmental conditions.[24,25] As can be seen in the graph, the ε' values rapidly decrease in the low-frequency region, while in the high-frequency region, they become nearly frequency independent. The Maxwell–Wagner polarisation model precisely explains this phenomenon, which is consistent with Koop's theory.[26] It was proposed that ferrites are composed of conducting grains (Gs) separated by resistive grain-boundaries (GBs). At low frequencies, the charge carrier moves from Gs to GBs, causing local lattice distortion due to the asymmetric charge distribution that travels along the applied field. This polarisation is referred to as space charge polarisation. However, as the frequency of the applied field increases, this slowly moving lattice distortion (space charge polarisation) cannot keep up and falls behind, resulting in a decrease in the ε' values with an increase in frequency.[27] Moreover, the figure

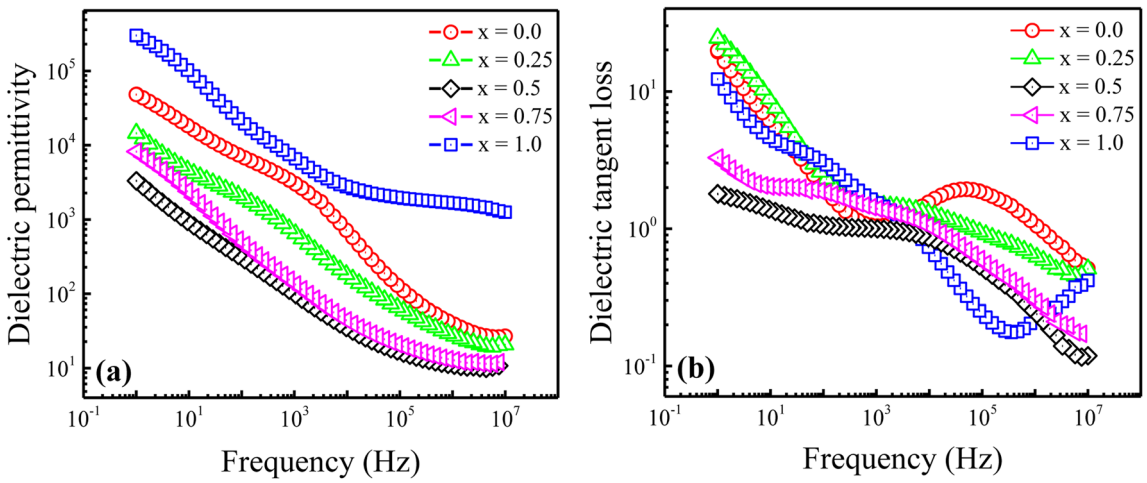

Fig. 4 Variation in (a) dielectric permittivity (ε') and (b) dielectric tangent loss ($\tan\delta$) *versus* frequency for the Ni^{2+}-doped $BaFe_{11}Cu_{1-x}Ni_xO_{19}$ hexaferrites with $x = 0.0$, 0.25, 0.5, 0.75, and 1.0.

demonstrates that the obtained value of ε' for the $BaFe_{11}Cu_1O_{19}$ sample (*i.e.*, $x = 0.0$) is comparably high compared to the pure $BaFe_{12}O_{19}$ sample prepared under similar conditions (not shown here) within the available frequency domain.[27] Here, the observed enhancement in ε' value can be attributed to the increase in electron transfer between the $Fe^{2+} \leftrightarrow Fe^{3+}$ ions to maintain the charge neutrality at the octahedral sites. However, with the incorporation of Ni^{2+} doping content up to $x = 0.5$, the initial decreasing trend of ε' may be due to the increase in the lattice strain (ε), which causes a distortion in the hexaferrite structure. This distortion may lead to a reduction in the concentration of intrinsic oxygen vacancies, which reduces the number of sites available for oxygen vacancies.[12] Consequently, the concentration of Fe^{2+} ions decreases with an increase in the Ni^{2+} doping content due to the fact that the intrinsic Fe^{2+} ions in $BaFe_{11}Cu_1O_{19}$ may transform into Fe^{3+} ions to achieve charge balance at the octahedral sites, which weakens the exchange of charges between the $Fe^{2+} \leftrightarrow Fe^{3+}$ ions, resulting in reduced values of ε' up to $x = 0.5$. Hence, the possible reason for this lower value of ε' is that at $x = 0.5$, the ratio of Cu^{2+} and Ni^{2+} ions reaches an optimum balance, where the concentration of oxygen vacancies and Fe^{2+} ions may be at their minimum in the system, resulting in a more stable lattice configuration and reduced polarization. However, a further increase in the Ni^{2+} doping content ($x > 0.5$) may cause a reversal in this trend and decrease the lattice strain. This decrease in lattice strain facilitates the formation of defects, including the creation of oxygen vacancies and the reduction of Fe^{3+} to Fe^{2+}. Therefore, the formation of Fe^{2+}/Fe^{3+} pair dipoles with an increase in the Ni^{2+} doping content begins to contribute to the permittivity of the prepared samples, resulting in an increase in ε' value for the $x >$ 0.5 samples. Moreover, the permittivity may also be affected by the transition of some of the Ni^{2+} ions to Ni^{3+} with an increase in the Ni^{2+} doping content.[16] Here, the ε' value was found to be highest for the $BaFe_{11}Ni_1O_{19}$ ($x = 1.0$) sample, which is ascribed to its highest dipole density (*i.e.*, Fe^{2+}/Fe^{3+} and Ni^{2+}/Ni^{3+}) among the prepared samples. This results in a colossal permittivity ($\sim 10^5$) for the $BaFe_{11}Ni_1O_{19}$ sample, which is two orders of magnitude higher than the permittivity of the pure $BaFe_{12}O_{19}$ sample and also among the highest reported values to date.[11,12,28]

The frequency dependence of the dielectric tangent loss ($\tan\delta$) for the Ni^{2+}-doped $BaFe_{11}Cu_{1-x}Ni_xO_{19}$ hexaferrites with $x =$ 0.0, 0.25, 0.50, 0.75, and 1.0 measured at room temperature is displayed in Fig. 4(b). As seen in the graph, the $\tan\delta$ values exhibit similar behaviour to that of dielectric permittivity. At lower frequencies, $\tan\delta$ has a higher magnitude because of the dominance of GBs, which inhibits the charge carrier hopping mechanism. Therefore, there is increased absorption, leading to greater loss. However, Gs are more conductive at higher frequencies because of the charge carrier hopping between the Fe^{2+}/Fe^{3+} and Ni^{2+}/Ni^{3+} ions at the octahedral site. Consequently, $\tan\delta$ is reduced given that there is less absorption at higher frequencies. Moreover, a dielectric relaxation peak was observed for all the samples, which indicates that the frequency at which electrons/holes hop between different ionic states is synchronized with the frequency of the applied alternating current.[29] However, as the Ni^{2+} doping concentration increases, the observed peaks shifted to a lower frequency, and the peak intensity decreased slightly. This peak shifting is due to the increased relaxation time of the polarizable entities in the prepared samples, which is influenced by the presence of additional dipoles introduced by the Ni^{2+} doping content. The obtained results suggest values of $\tan\delta$ <1.0 at higher frequencies (10^5–10^7 Hz). Among the prepared samples, the reduced $\tan\delta$ value for the $x = 1.0$ sample together with the colossal ε' value makes this composition attractive for high-frequency applications.

Fig. 5 displays the variation in AC conductivity (σ_{ac}) with applied frequency for the prepared Ni^{2+}-doped $BaFe_{11}Cu_{1-x}Ni_xO_{19}$ hexaferrites with $x = 0.0$, 0.25, 0.50, 0.75, and 1.0 measured at room temperature. Typically, the microscopic motion of charge carriers within the hexagonal ferrites can be inferred from the frequency (f) *vs.* AC conductivity (σ_{ac}) plot. As

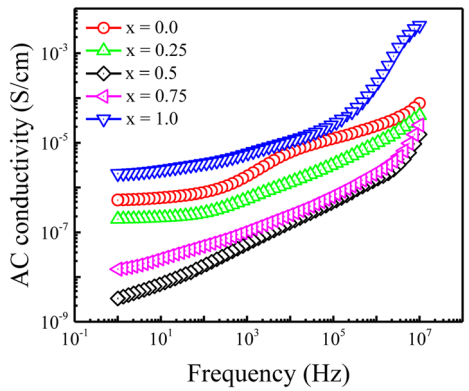

Fig. 5 Frequency-dependent AC conductivity (σ_{ac}) for Ni^{2+}-doped $BaFe_{11}Cu_{1-x}Ni_xO_{19}$ hexaferrites with x = 0.0, 0.25, 0.5, 0.75, and 1.0.

seen in the figure, the behaviour of σ_{ac} shows the opposite dependence on frequency as that of ε' and $\tan\delta$. Here, the conductivity increases with an increase in frequency for all the samples. The values of σ_{ac} are small at lower frequencies and high at higher frequencies. It is well known that electron hopping between Fe^{2+} and Fe^{3+} ions is the key factor that determines the conductivity of hexaferrites and this electron hopping is strongly dependent on the concentration of Fe^{2+} and Fe^{3+} ions at the octahedral site.[24] This hopping process increases with an increase in frequency, making conductive Gs more dominant, and hence the conductivity increases. Thus, to understand the observed dispersive behaviour of the conductivity graphs, the obtained data was fitted with Jonscher's power law, as follows:[30]

$$\sigma_{ac}(\omega) = \sigma_o + A\omega^n \quad (2)$$

where σ_o denotes the frequency-independent component of conductivity, A is a constant that defines the polarizability strength, ω is the angular frequency, and n is the slope of the frequency-dependent curve ($0 \le n \le 1$). Table 2 presents the values of the various fitted parameters. Further, the figure shows that the value of σ_{ac} initially decreases with an increase in Ni^{2+} doping content up to $x = 0.5$, and thereafter it begins to increase for $x > 0.5$. Here, the observed variation in the values of σ_{ac} depends on the dopant concentration (x), which alters the Fe^{2+}/Fe^{3+} ratio in the prepared samples (as discussed earlier), resulting in a variation in the conductivity. According to the obtained results, the $BaFe_{11}Ni_1O_{19}$ ($x = 1.0$) sample has the highest σ_{ac} value and lowest n value among the prepared samples. Moreover, the obtained values of σ_{ac} for the $x = 1.0$ sample were found to be two orders of magnitude higher than the permittivity of the pure $BaFe_{12}O_{19}$ sample in the available frequency range. This behavior can be due to comparatively increased $Fe^{2+} \leftrightarrow Fe^{3+}$ and $Ni^{2+} \leftrightarrow Ni^{3+}$ conducting networks and dense microstructures.

The Nyquist plane plots of the prepared Ni^{2+}-doped $BaFe_{11}Cu_{1-x}Ni_xO_{19}$ hexaferrites with $x = 0.0$, 0.25, 0.50, 0.75, and 1.0 measured at room temperature are shown in Fig. 6. Typically, the Nyquist plane plot consists of one or more completely resolved or poorly resolved semi-circles, depending on the number of dielectric relaxation processes or crystallographic phases present in the produced samples. In our single-phase produced samples, we observed two poorly resolved semi-circles with dissimilar widths. These semi-circles correspond to separate dielectric relaxation processes, namely Gs and GBs. We used the ZView software to fit our experimental data with an equivalent circuit model to further analyze the Nyquist plane plots. The components of the applied circuit were (R_1Q_1) and ($R_2Q_2C_3$) linked in series, where R_1 and R_2 are the resistance, C_1 and C_3 are the capacitance, and Q_1 and Q_2 are the constant phase elements reflecting the capacitance variation from the optimal dielectric behavior. The following formulas were used to calculate the capacitance of each constant-phase element:[31]

$$C = Q^{1/n}R^{(1-n/n)} \quad (3)$$

where n denotes the degree to which the capacitance deviates from the ideal resistive ($n = 0$) or capacitive ($n = 1$) behavior. The values of the various derived components are listed in Table 2 according to the result of the synchronizing experimental data with fitting. According to the analysis of the fitted data, we found that lower values of R_1 are obtained from the first circuit (R_1Q_1), while the estimated capacitance values (C_1) using Q_1 (eqn (3)) are within the Gs geometrical capacitance range (10^{-11}–10^{-13} F cm^{-1}).[32] Thus, the semi-circles in the higher frequency zone are correlated with the dielectric relaxation of Gs. However, we found significantly greater values of R_2 from the second circuit ($R_2Q_2C_3$), while the estimated values of capacitance (C_2) using Q_2 (eqn (3)) are within the geometrical capacitance range of GBs (10^{-8}–10^{-10} F cm^{-1}).[32] Therefore, the semi-circles in the lower frequency zone are ascribed to the dielectric relaxation of GBs, but the values of C_3 are linked to the presence of space charges surrounding Gs, which may create an interface that impedes charge carrier movement. Due to the

Table 2 Fitted parameters of the Jonscher power law (σ_o, n) and Nyquist plots (R_1, C_1, R_2, C_2, C_3, and R_T) for $BaFe_{11}Cu_{1-x}Ni_xO_{19}$ hexaferrites

	Jonscher power law				Equivalent circuit model			
Samples (x)	σ_o	n	R_1 (Ω)	C_1 (F)	R_2 (Ω)	C_2 (F)	C_3 (F)	R_T (Ω)
0.0	3.55×10^{-6}	0.66	2.75×10^{4}	4.50×10^{-12}	4.37×10^{5}	2.93×10^{-9}	6.25×10^{-11}	4.65×10^{5}
0.25	5.24×10^{-8}	0.52	7.05×10^{5}	3.14×10^{-11}	3.19×10^{7}	9.41×10^{-9}	5.82×10^{-12}	3.26×10^{7}
0.5	8.10×10^{-9}	0.50	1.75×10^{7}	1.17×10^{-11}	4.19×10^{8}	4.12×10^{-8}	3.95×10^{-12}	4.36×10^{8}
0.75	2.37×10^{-7}	0.48	1.46×10^{5}	7.17×10^{-12}	1.09×10^{6}	1.07×10^{-9}	1.79×10^{-11}	1.23×10^{6}
1.0	1.78×10^{-6}	0.26	1.74×10^{4}	3.97×10^{-11}	1.36×10^{5}	5.21×10^{-8}	7.68×10^{-11}	1.53×10^{5}

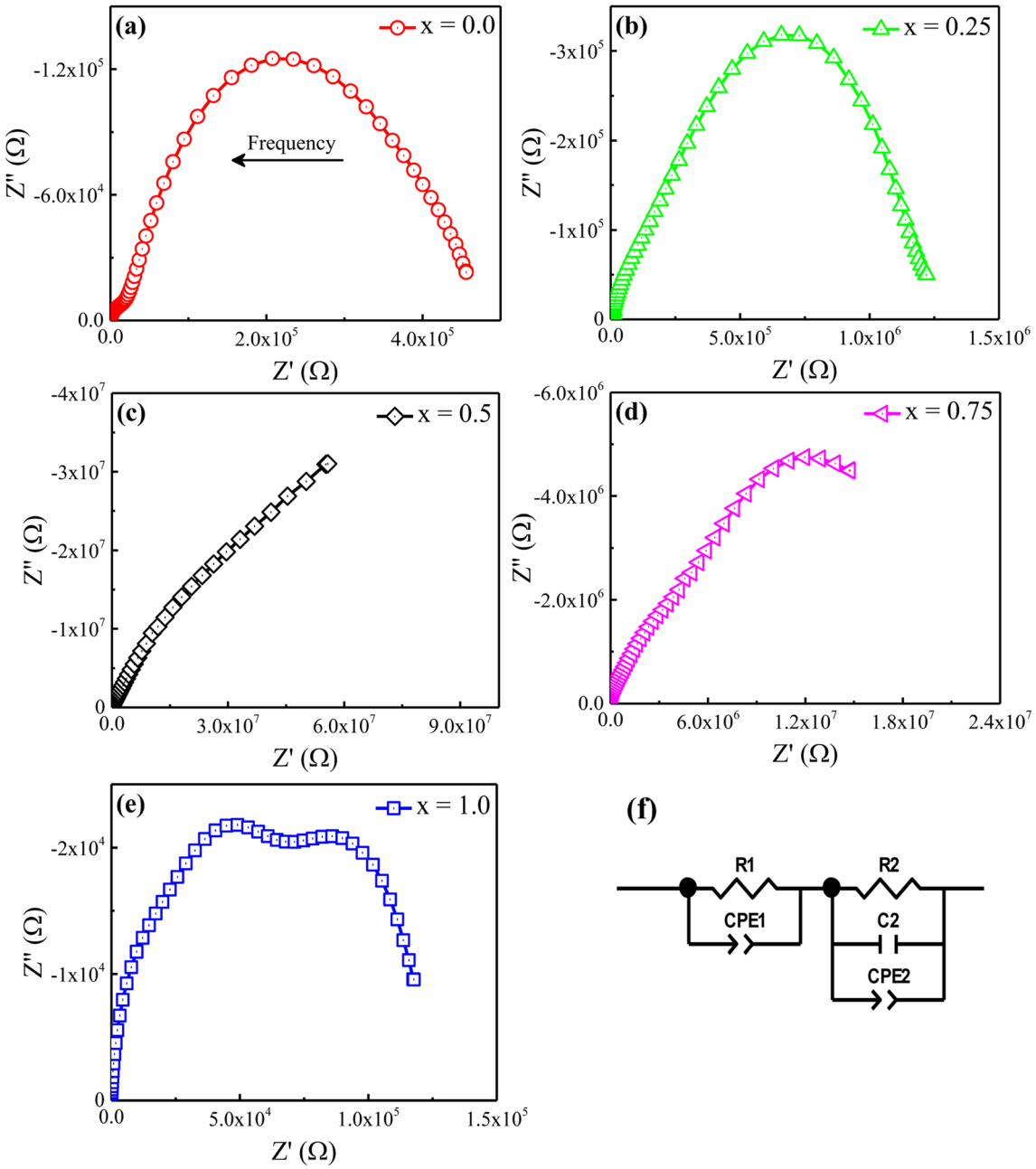

Fig. 6 (a–e) Nyquist plane plots (Z' *vs.* Z'') for the prepared Ni^{2+}-doped $BaFe_{11}Cu_{1-x}Ni_xO_{19}$ hexaferrites with $x = 0.0$, 0.25, 0.50, 0.75, and 1.0. (f) Equivalent circuit model used for fitting experimental data. Arrow in (a) points to the direction of increasing frequency.

localization of these space charges, these hexaferrites produce high dielectric permittivity values.[24] Additionally, Table 2 includes the total resistance of the prepared sample ($R_T = R_{Gs} + R_{GBs}$). It was found that initially R_T increases significantly with an increase in the Ni^{2+} doping content up to $x = 0.5$, and afterwards it decreases for $x > 0.5$. Here, the observed increase in R_T with x based on the decrease in the grain size and Fe^{2+}/Fe^{3+} ratio results in an overall decline in conductivity; thus, an increase in R_T was observed up to the $x = 0.5$ sample. However, in the case of $x > 0.5$, the observed decreasing trend of R_T is due to the increase in grain size and Fe^{2+}/Fe^{3+} ratio together with the availability of an additional hopping network ($Ni^{2+} \leftrightarrow Ni^{3+}$) to facilitate the conduction mechanism, as discussed earlier.

Fig. 7(a) displays the magnetic hysteresis loops of the Ni^{2+}-doped $BaFe_{11}Cu_{1-x}Ni_xO_{19}$ hexaferrites with $x = 0.0$, 0.25, 0.50, 0.75, and 1.0 measured at room temperature under an applied magnetic field of ±20 kOe. The saturation magnetization (M_s), remanence magnetization (M_r), and coercivity (H_c) values of all the prepared samples were obtained using these hysteresis loops. The obtained values for these parameters are listed in Table 3. As can be observed, the magnetic characteristics changed significantly with the dopant concentration in the

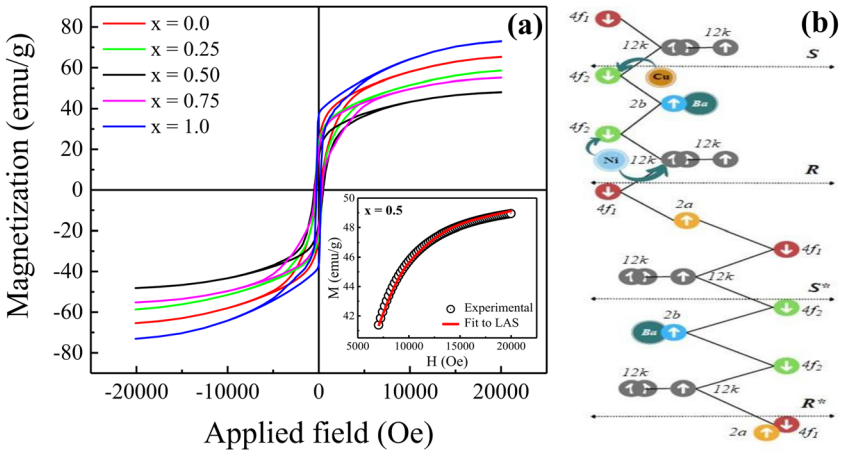

Fig. 7 (a) Magnetic hysteresis loops of Ni^{2+}-doped $BaFe_{11}Cu_{1-x}Ni_xO_{19}$ hexaferrites with x = 0.0, 0.25, 0.50, 0.75, and 1.0. Inset shows a representative LAS curve for the $x = 0.5$ sample. (b) Schematic representation of the occupation of cations in M-type hexaferrites. The black, red, and green spheres represent Fe ions. The directional arrows represent the local magnetic moments of atomic positions.

$BaFe_{11}Cu_{1-x}Ni_xO_{19}$ hexaferrites due to the preferential occupancy of the Cu^{2+} and Ni^{2+} ions at different crystellographic sites. As shown in Fig. 7(b), the magnetic moment of $BaFe_{12}O_{19}$, which is typically deduced by analyzing the difference in magnetic moments between the crystallographic sites, was measured to be 20 μ_B (*i.e.*, $M = M(12k + 2a + 2b)\uparrow - M(4f_1 + 4f_2)\downarrow$).[18,33] Here, the M_s value for the prepared $BaFe_{11}Cu_1O_{19}$ sample ($x = 0.0$) was found to be 65 emu g^{-1}, which is comparatively higher than that of the pure $BaFe_{12}O_{19}$ sample (*i.e.*, 55 emu g^{-1}) prepared under similar conditions. This observed improvement in M_s value for the $x = 0.0$ sample can be understood based on the fact that the comparatively less magnetic Cu^{2+} (1 μ_B) ions replace the Fe^{3+} (5 μ_B) ions at their preferential $4f_2$ spin-down site and convert more Fe^{3+} into Fe^{2+} ions at the octahedral sites due to charge compensation. Therefore, the magnetic moment on the spin-down site decreases, leading to an increase in the M_s value for the $BaFe_{11}Cu_1O_{19}$ compared to the $BaFe_{12}O_{19}$ sample.[34] However, upon the incorporation of Ni^{2+} (2 μ_B) ions in place of Cu^{2+} (1 μ_B) ions in the $BaFe_{11}Cu_{1-x}Ni_xO_{19}$ hexaferrites, we found that the value of M_s initially decreased with an increase in the Ni^{2+} doping content up to $x = 0.5$, and thereafter it increased. Here, the observed initial decrease in the M_s value with an increase in Ni^{2+} content may be related to the decrease of the net magnetic moment per formula unit, indicating the preferential occupation of Ni^{2+} at the 12k spin-up and $4f_2$ spin-down sites, while the Cu^{2+} ions occupy the $4f_2$ spin-down site in the place of the Fe^{3+} ions (see Fig. 7(b)). Thus, the difference in magnetic moments across the sites decreases, leading to a decline in the M_s value from 65 emu g^{-1} ($x = 0.0$) to 50 emu g^{-1} ($x = 0.5$). However, when the Ni^{2+} doping content exceeded $x = 0.5$, the Ni^{2+} ions gradually occupied the $4f_2$ spin-down sites, while the Cu^{2+} ions take up the $4f_2$ site together with reducing more Fe^{3+} ions to Fe^{2+} ions. This leads to an increase in the difference between the sites, and thus the value of M_s increases from 50 emu g^{-1} ($x = 0.5$) to 73 emu g^{-1} ($x = 1.0$). Among the produced samples, the highest value of M_s was obtained for the $BaFe_{11}Ni_1O_{19}$ sample ($x = 1.0$), which is found to be higher than the reported values,[12] where the respective value of M_s decreases at a higher Ni^{2+} content due to the formation of a secondary phase having comparatively weak magnetic nature. Furthermore, the magnetic anisotropy (K_1) of the prepared samples was estimated by employing the law of approach to magnetic saturation (LAS), which can be expressed as follows:[35,36]

$$M(H) = M_s\left(1 - \frac{b}{H^2}\right) \quad (4)$$

where M_s denotes the saturation magnetization, H denotes the magnetic field, and b denotes the anisotropy parameter. In the case of M-type hexagonal symmetry, b can be computed using the following expression:

$$b = \frac{4K_1^2}{15M_s^2} \quad (5)$$

The inset of the figure shows the fitting of the high-field region (*i.e.*, $H \gg H_c$) of the representative hysteresis loop of the $x = 0.5$ sample. According to the values of the fitting parameters (M_s and b), the values of K_1 for the prepared samples were calculated. As shown in Table 3, the value of K_1 initially decreased, and then increased with an increase in the Ni^{2+} doping content, reaching a minimal value at $x = 0.5$. In M-type hexaferrites, the 12k, $4f_2$, and 2b sites are known as major

Table 3 Variation in saturation magnetization (M_s), remnant magnetization (M_r), coercivity (H_c), and anisotropy constant (K_1) with x in $BaFe_{11}Cu_{1-x}Ni_xO_{19}$ hexaferrites

Sample (x)	M_s (emu g^{-1})	M_r (emu g^{-1})	H_c (Oe)	$K_1 \times 10^5$ (erg g^{-1})
0.0	65	24	238	3.87
0.25	58	22	430	3.44
0.5	49	16	500	2.71
0.75	55	20	387	3.10
1.0	73	35	222	4.53

Table 4 Saturation magnetization (M_s) and dielectric parameters (ε' and tan δ) at a representative frequency (f) from other studies compared to our results measured at room temperature

Composition	M_s (emu g^{-1})	Dielectric parameters			Reference
		f (Hz)	ε'	tan δ	
$BaFe_{12}O_{19}$ (18–65 nm)	18–51	10 MHz	<50	<0.2	40
$BaFe_{12-x}Co_xO_{19}$ (x = 0.0, 0.05, 0.1, 0.2)	75.36–56.08	10 MHz	400–300	<0.2	41
$BaFe_{12-2x}Co_xSm_xO_{19}$ (x = 0.0, 0.2, 0.4, 0.6)	51.17–80.20	3 MHz	7.42–5.06	<0.05	42
$Ba_{1-x}Ce_xFe_{12-x}Co_xO_{19}$ (x = 0.0–0.2)	46–37	1 GHz	3.8–2.2	<0.5	43
$BaFe_{12-x}Ni_xO_{19}$ (x = 0, 0.1, 0.2, 0.3, 0.4, 0.5)	68–59	10 MHz	∼100	<1.0	11
$BaFe_{12-2x}Ni_xO_{19}$ (x = 0, 0.3, 0.5)	55.35–57.57	1 MHz	90–150	<0.1	28
$Ba_{1-x}Nd_xFe_{12-y}Cu_yO_{19}$ (x,y = 0.0, 0.15, 0.30, 0.45, 0.60)	68.4–42.3	10 MHz	150–300	<1.0	44
$BaCu_xCr_xFe_{12-2x}O_{19}$ ($0.0 \leq x \leq 0.5$)	50.84–68.99	1 MHz	8–16	<0.2	45
$BaFe_{12-2x}Ni_xZr_xO_{19}$ ($0.0 \leq x \leq 1.0$)	71.5–20.5	1 MHz	300–930	<1.0	16
$BaFe_{11}Ni_1O_{19}$	73	10 MHz	1300	0.4	This work
$BaFe_{11}Cu_1O_{19}$	65		30	0.45	

contributors to the magnetic anisotropy.[37] Therefore, the initial decrease observed in the K_1 value is attributed to the competition between the Ni^{2+} and Cu^{2+} ions to occupy the 12k, $4f_2$ and $4f_2$ sites in place of Fe^{3+} ions, respectively, thereby weakening the magnetic anisotropy. However, the observed increase in K_1 for $x > 0.5$ can be explained by the probable occupation of the Ni^{2+} and Cu^{2+} ions at the $4f_2$ site, which transfer more Fe^{3+} ions from the octahedral to tetrahedral sites, thus increasing the magnetic anisotropy. Moreover, the variation in coercivity (H_c) with an increase in the Ni^{2+} doping content can be related to the changes in magnetic anisotropy (K_1) and grain size (G) of the prepared hexaferrites (see Table 1). Here, we found that H_c has a positive relationship with K_1 and inverse dependance on G.[38,39]

Table 4 shows a comparison of the magnetic and dielectric characteristics of the prepared $BaFe_{11}Cu_{1-x}Ni_xO_{19}$ hexaferrites (x = 0.0 and 1.0) with the reported relevant compositions measured at room temperature. The comparison reveals that the fabricated sample $BaFe_{11}Ni_1O_{19}$ (x = 1.0) exhibits comparatively high values of saturation magnetization (M_s) and dielectric permittivity (ε') together with a low dielectric tangent loss (tan δ). This is probably because of the influence of the Ni^{2+} ions occupying the $4f_2$ sites and the increased dipole density (Fe^{2+}/Fe^{3+}). Therefore, the coexistence of high magnetic saturation and dielectric permittivity in the $BaFe_{11}Ni_1O_{19}$ material presents potential for its utilization in microwave-absorbing devices. This highlights its application in new technologies and helps advance materials that are designed to effectively attenuate electromagnetic waves.

4. Conclusions

In this study, we investigated the effect of Ni^{2+}–Cu^{2+} co-doping on the structural, dielectric, and magnetic characteristics of barium hexaferrites. The co-precipitation technique was employed to prepare Ni^{2+}–Cu^{2+} co-doped $BaFe_{11}Cu_{1-x}Ni_xO_{19}$ hexaferrites with x = 0.0, 0.25, 0.50, 0.75, and 1.0. All the prepared samples showed the development of a single-phase hexagonal structure, according to the Rietveld refinement of their XRD patterns. The structural analysis revealed that doping of Ni^{2+} and Cu^{2+} changed the values of the lattice parameters (a,c), unit-cell volume, lattice strain, and crystallite size, which were explained in terms of the difference in the ionic radii and occupation at the different crystallographic sites. The FE-SEM analysis showed that the grains are hexagonal in shape, while EDX confirmed the stoichiometry of the produced samples. The XPS analysis confirmed the formation of Fe^{2+} ions; however, the ratio of Fe^{2+}/Fe^{3+} changed with an increase in the Ni^{2+} doping content. Dielectric measurements displayed a decreasing trend in the frequency-dependent dielectric behavior, in accordance with Maxwell–Wagner interfacial polarization. Alternatively, the impedance analysis showed a considerable variation in the resistive properties of the prepared samples with an increase in the Ni^{2+}–Cu^{2+} doping content. The observed variation in the dielectric and resistive properties were attributed to the changes in the grain size and electron–hole transfer between the charge carriers. The magnetic measurements showed that the Ni^{2+}–Cu^{2+} co-doping caused a noticeable variation in the values of M_s and H_c measured at room temperature. This was attributed to the preferential occupation of the Ni^{2+} ions at the different crystallographic sites, which may have a more significant impact on the overall magnetic moment. Based on the obtained results, we found that the sample with x = 1.0 had the highest dielectric permittivity (>10^3 at 10^7 Hz) and magnetization (73 emu g^{-1}) together with a lowest dielectric tangent loss (0.2) and material resistance (1.5×10^5 Ω). This makes the $BaFe_{11}Ni_1O_{19}$ composition a promising choice as a microwave absorption material, which requires high dielectric permittivity and magnetization together with a reduced dielectric tangent loss. Currently, experiments are being conducted to measure the electromagnetic interference (EMI) shielding efficacy of this material. In the future, we are planning to disperse $BaFe_{11}Ni_1O_{19}$ in a conductive matrix to develop a light-weight, flexible, and efficient composite material for microwave absorbing applications.

Author statement

M. Atif: conceptualization, supervision, writing – review & editing. H. Ul Husnain: investigation, data curation, writing – original draft. Atta Ur Rehman: investigation, visualization, formal analysis. U. Younas: investigation, formal analysis. T. Rafique: investigation, formal analysis. W. Khalid: software, validation. Z. Ali: writing – review & editing. M. Nadeem: conceptualization, resources.

Conflicts of interest

There are no conflicts to declare.

References

1 L. A. Dobrzański, M. Drak and B. Zębowicz, Materials with specific magnetic properties, *J. Achiev. Mater. Manuf. Eng.*, 2006, **17**, 37–40.

2 L. Deng, Y. Zhao, Z. Xie, Z. Liu, C. Tao and R. Deng, Magnetic and microwave absorbing properties of low-temperature sintered $BaZr_xFe_{12-x}O_{19}$, *RSC Adv.*, 2018, **8**, 42009–42016.

3 R. C. Pullar, Hexagonal ferrites: a review of the synthesis, properties and applications of hexaferrite ceramics, *Prog. Mater. Sci.*, 2012, **57**, 1191–1334.

4 P. Campbell, *Permanent Magnet Materials and Their Application*, Cambridge University Press, Cambridge, 1994.

5 B. J. Evans, F. Grandjean, A. P. Lilot, R. H. Vogel and A. Gérard, ^{57}Fe hyperfine interaction parameters and selected magnetic properties of high purity $MFe_{12}O_{19}$ (M = Sr, Ba), *J. Magn. Magn. Mater.*, 1987, **67**, 123–129.

6 R. A. McCurrie, *Ferromagnetic Materials: Structure and Properties*, Academic Press Limited, London, 1994.

7 R. Valenzuela, Novel Applications of Ferrites, *Phys. Res. Int.*, 2012, **2012**, 591839.

8 A. V. Trukhanov, V. G. Kostishyn, L. V. Panina, V. V. Korovushkin, V. A. Turchenko, P. Thakur, A. Thakur, Y. Yang, D. A. Vinnik, E. S. Yakovenko, L. Yu. Matzui, E. L. Trukhanova and S. V. Trukhanov, Control of electromagnetic properties in substituted M-type hexagonal ferrites, *J. Alloys Compd.*, 2018, **754**, 247–256.

9 H. Kojima, Fundamental properties of hexagonal ferrites with magnetoplumbite structure, *Handbook of Ferromagnetic Materials*, Elsevier, 1982, vol. 3, pp. 305–391.

10 M. K. Manglam, S. Kumari, L. K. Pradhan, S. Kumar and M. Kar, Lattice strain caused magnetism and magnetocrystalline anisotropy in Zn modified barium hexaferrite, *Phys. B*, 2020, **588**, 412200.

11 P. Behera and S. Ravi, Effect of Ni doping on structural, magnetic and dielectric properties of M-type barium hexaferrite, *Solid State Sci.*, 2019, **89**, 139–149.

12 M. Wang, Q. Xu, S. Wang, Z. Wang, N. Ma and P. Du, Formation of $BaFe_{12-x}Ni_xO_{19}$ ceramics with considerably high dielectric and magnetic property coexistence, *J. Alloys Compd.*, 2018, **765**, 951–960.

13 S. Kumar, S. Guha, S. Supriya, L. K. Pradhan and M. Kar, Correlation between crystal structure parameters with magnetic and dielectric parameters of Cu-doped barium hexaferrite, *J. Magn. Magn. Mater.*, 2020, **499**, 166213.

14 Widyastuti, N. Sasria, A. M. Alviani, M. D. Febri R. and V. Mitha P., Ni and Zn Substituted M-type Barium Hexaferrite Processed by Sol–Gel Auto Combustion Method, *J. Phys.: Conf. Ser.*, 2017, **877**, 012015.

15 Susilawati, A. Doyan, H. Khair, M. Taufik and Wahyudi, Electrical, Magnetic and Microwave Absorption Properties of M-type Barium Hexaferrites ($BaFe_{12-2x}Co_xNi_xO_{19}$), *J. Phys.: Conf. Ser.*, 2018, **1011**, 012009.

16 Y. Zou, J. Lin, W. Zhou, M. Yu, J. Deng, Z. Chen, G. Luo and D. Wang, Coexistence of high magnetic and dielectric properties in Ni-Zr co-doped barium hexaferrites, *J. Alloys Compd.*, 2022, **907**, 164516.

17 M. Amini and A. Gholizadeh, Shape control and associated magnetic and dielectric properties of $MFe_{12}O_{19}$ (M = Ba, Pb, Sr) hexaferrites, *J. Phys. Chem. Solids.*, 2020, **147**, 109660.

18 M. Atif, S. Ullah, A. Ur Rehman, K. Shahzad, W. Khalid, Z. Ali, Y. Chen, H. Guo and M. Nadeem, Structural, magnetic, and dielectric properties of Ti^{4+}–M^{2+} co-doped $BaFe_{11}Ti_{0.5}M_{0.5}O_{19}$ hexaferrites (M = Co^{2+}, Ni^{2+}, Zn^{2+}), *Ceram. Int.*, 2021, **47**, 15245–15252.

19 R. D. Shannon, Revised effective ionic radii and systematic studies of interatomic distances in halides and chalcogenides, *Acta Crystallogr. A*, 1976, **32**, 751–767.

20 M. J. Iqbal, M. Naeem Ashiq and P. Hernandez-Gomez, Effect of annealing temperature and substitution of Zr-Cu onmagnetic properties of strontium hexaferrite nanoparticles, *J. Phys.: Conf. Ser.*, 2009, **153**, 012053.

21 M. A. Almessiere, Y. Slimani, N. A. Tashkandi, A. Baykal, M. F. Saraç, A. V. Trukhanov, I. Ercan, I. Belenli and B. Ozçelik, The effect of Nb substitution on magnetic properties of $BaFe_{12}O_{19}$ nanohexaferrites, *Ceram. Int.*, 2019, **45**, 1691–1697.

22 G. K. Williamson and W. H. Hall, X-ray line broadening from filed aluminium and wolfram, *Acta Mater.*, 1953, **1**, 22–31.

23 S. Vadivelan and N. Victor Jaya, Investigation of magnetic and structural properties of copper substituted barium ferrite powder particles via co-precipitation method, *Results Phys.*, 2016, **6**, 843–850.

24 M. Atif, M. H. Alvi, S. Ullah, A. Ur Rehman, M. Nadeem, W. Khalid, Z. Ali and H. Guo, Impact of strontium substitution on the structural, magnetic, dielectric and ferroelectric properties of $Ba_{1-x}Sr_xFe_{11}Cr_1O_{19}$ (x = 0.0–0.8) hexaferrites, *J. Magn. Magn. Mater.*, 2020, **500**, 166414.

25 B. Unal, M. A. Almessiere, A. V. Trukhanov, A. Baykal, Y. Slimani, M. V. Silibin, A. Ul-Hamid and A. Manikandan, A study on the conductivity, dielectric, and microwave properties of $SrNb_xY_xFe_{12-2x}O_{19}$ ($0.00 \leq x \leq 0.05$) nanohexaferrites, *J. Mater. Res. Technol.*, 2022, **17**, 2975–2986.

26 K. W. Wagner, The distribution of relaxation times in typical dielectrics, *Ann. Phys.*, 1993, **40**, 817–819.

27 N. Raghuram, T. Subba Rao and K. Chandra Babu Naidu, Electrical and impedance spectroscopy properties of hydrothermally synthesized $Ba_{0.2}Sr_{0.8-y}La_yFe_{12}O_{19}$ (y = 0.2 – 0.8) nanorods, *Ceram. Int.*, 2020, **46**, 5894–5906.

28 M. A. Rafiq, M. Waqar, T. A. Mitza, A. Farooq and A. Zulfiqar, Effect of Ni^{2+} Substitution on the Structural, Magnetic, and Dielectric Properties of Barium Hexagonal Ferrites ($BaFe_{12}O_{19}$), *J. Electron. Mater.*, 2017, **46**, 241–246.
29 T. Rafique, M. Atif, A. Ur Rehman, H. Wahab, W. Khalid, Z. Ali and M. Nadeem, Colossal permittivity, resistive and magnetic properties of zinc substituted manganese ferrites, *J. Alloys Compd.*, 2022, **923**, 166454.
30 A. K. Jonscher, *Dielectric Relaxations in Solids*, Chelsea Dielectrics, London, 1983.
31 E. Barsoukov and J. R. Macdonald, *Impedance Spectroscopy Theory, Experiments and Applications*, Wiley, New York, 2005.
32 J. T. S. Irvine, D. C. Sinclair and A. R. West, Electroceramics: characterization by impedance spectroscopy, *Adv. Mater.*, 1990, **2**, 132.
33 S. Caliskan, M. A. Almessiere, A. Baykal, Y. Slimani, H. Gungunes, A. Demir Korkmaz, A. Ul-Hamid and I. A. Auwal, Magnetic properties of $Sr_{0.5}Ba_{0.5}Ho_xFe_{12-x}O_{19}$ ($x \leq 0.10$) nanohexaferrites, *Appl. Phys. A*, 2023, **129**, 616.
34 M. A. Rafiq, M. Waqar, Q. K. Muhammad, M. Waleed, M. Saleem and M. S. Anwar, Conduction mechanism and magnetic behavior of Cu doped barium hexaferrite ceramics, *J. Mater. Sci.: Mater. Electron.*, 2018, **29**, 5134–5142.
35 M. A. Almessiere, Y. Slimani, H. S. El Sayed, A. Baykal and I. Ercan, Microstructural and magnetic investigation of vanadium-substituted Sr-nanohexaferrite, *J. Magn. Magn. Mater.*, 2019, **471**, 124–132.
36 O. Ramanjaneyulu, N. Suresh Kumar, D. Baba Basha and K. Chandra Babu Naidu, Structural, thermal, magnetic, and electrical properties of $Ba_{1-x}Cu_xFe_{12}O_{19}$ ($x = 0.2$–0.8) nanoparticles, *J. Mater. Sci.: Mater. Electron.*, 2023, **34**, 449.
37 Z. Yang, C. S. Wang, X. H. Li and H. X. Zeng, (Zn, Ni, Ti) substituted barium ferrite particles with improved temperature coefficient of coercivity, *Mater. Sci. Eng. B.*, 2002, **90**, 142–145.
38 J. Chen, Z. Wang, Z. Cheng, Z. Shi, X. Deng, Y. Chen, Y. Zou, G. Luo and W. Zhou, Investigation on the structural, magnetic, and dielectric properties of Ni^{2+}–Zr^{4+} co-doped Y-type hexaferrite $Ba_2Ni_2Fe_{12}O_{22}$, *J. Mater. Sci.: Mater. Electron.*, 2022, **33**, 16889–16898.
39 A. Gholizadeh and V. Banihashemi, Effects of Ca–Gd co-substitutionon the structural, magnetic, and dielectricproperties of M-type strontium hexaferrite, *J. Am. Ceram. Soc.*, 2023, **106**, 5351–5363.
40 S. Kumar, S. Supriya, L. K. Pradhan, R. Pandey and M. Kar, Grain size effect on magnetic and dielectric properties of barium hexaferrite (BHF), *Phys. B*, 2020, **579**, 411908.
41 A. Kumar, M. K. Verma, S. Singh, T. Das, L. Singh and K. D. Mandal, Electrical, Magnetic and Dielectric Properties of Cobalt-Doped Barium Hexaferrite $BaFe_{12-x}Co_xO_{19}$ ($x = 0.0$, 0.05, 0.1, and 0.2) Ceramic Prepared via a Chemical Route, *J. Electron. Mater.*, 2020, **49**, 6436–6447.
42 G. Asghar, S. Asri, S. N. Khusro, G. H. Tariq, M. S. Awan, M. Irshad, A. Safeen, Z. Iqbal, W. H. Shah and M. Anis-ur-Rehman, Enhanced Magnetic Properties of Barium Hexaferrite, *J. Electron. Mater.*, 2020, **49**, 4318–4323.
43 Z. Lalegani and A. Nemati, Effects of Ce–Co substitution on structural, magnetic and dielectric properties of M-type barium hexaferrite nanoparticles synthetized by sol–gel auto-combustion route, *J. Mater. Sci.: Mater. Electron.*, 2015, **26**, 2134–2144.
44 F. Bibi, S. Iqbal, H. Sabeeh, T. Saleem, B. Ahmad, M. Nadeem, I. Shakir, M. Aadil and A. Kalsoom, Evaluation of structural, dielectric, magnetic and photocatalytic properties of Nd and Cu co-doped barium hexaferrite, *Ceram. Int.*, 2021, **47**, 30911–30921.
45 A. A. Gor, N. M. Devashrayee, T. Gupta, C. C. Chauhan and R. B. Jotania, A study of the effect of the Cu and Cr co-doping on structural, magnetic and dielectric properties of barium hexaferrites synthesized in presence of mentha leaves extract, *Mater. Today Commun.*, 2023, **37**, 107214.